Lawrence Berkeley National Laboratory
LBL Publications

Title
Lithium-excess olivine electrode for lithium rechargeable batteries

Permalink
https://escholarship.org/uc/item/4tw7r00c

Journal
Energy & Environmental Science, 9(9)

ISSN
1754-5692

Authors
Park, Kyu-Young
Park, Inchul
Kim, Hyungsub
et al.

Publication Date
2016

DOI
10.1039/c6ee01266c

Peer reviewed

Energy & Environmental Science

PAPER

Lithium-excess olivine electrode for lithium rechargeable batteries†

Kyu-Young Park,[ab] Inchul Park,[ab] Hyungsub Kim,[abc] Gabin Yoon,[a] Hyeokjo Gwon,[d] Yongbeom Cho,[a] Young Soo Yun,[e] Jung-Joon Kim,[a] Seongsu Lee,[c] Docheon Ahn,[f] Yunok Kim,[g] Haegyeom Kim,‡[a] Insang Hwang,[a] Won-Sub Yoon[g] and Kisuk Kang*[ab]

Lithium iron phosphate (LFP) has attracted tremendous attention as an electrode material for next-generation lithium-rechargeable battery systems due to the use of low-cost iron and its electrochemical stability. While the lithium diffusion in LFP, the essential property in battery operation, is relatively fast due to the one-dimensional tunnel present in the olivine crystal, the tunnel is inherently vulnerable to the presence of Fe_{Li} anti-site defects (Fe ions in Li ion sites), if any, that block the lithium diffusion and lead to inferior performance. Herein, we demonstrate that the kinetic issue arising from the Fe_{Li} defects in LFP can be completely eliminated in lithium-excess olivine LFP. The presence of an excess amount of lithium in the Fe ion sites (Li_{Fe}) energetically destabilizes the Fe_{Li}-related defects, resulting in reducing the amount of Fe defects in the tunnel. Moreover, we observe that the spinodal decomposition barrier is notably reduced in lithium-excess olivine LFP. The presence of Li_{Fe} and the absence of Fe_{Li} in lithium-excess olivine LFP additionally induce faster kinetics, resulting in an enhanced rate capability and a significantly reduced memory effect. The lithium-excess concept in the electrode crystal brings up unexpected properties for the pristine crystal and offers a novel and interesting approach to enhance the diffusivity and open up additional diffusion paths in solid-state ionic conductors.

Broader context

This work provides a fresh perspective on $LiFePO_4$ olivine, one of the most important cathode materials for next-generation lithium rechargeable batteries, by introducing a new class of 'lithium-excess $Li_{1+x}Fe_{1-x}PO_4$'. The lithium-excess olivine shows unexpected physical and chemical properties remarkably distinguishable from conventional $LiFePO_4$, such as near-zero Fe_{Li} related defects, a new [101] lithium diffusional path, a lower spinodal decomposition barrier and a reduced memory effect. Most importantly, our work demonstrates that the lithium-excess concept can be applied to not only layered type electrode materials but also polyanion-based electrodes, suggesting that the lithium-excess strategy could be adopted for various crystal structures and would open a new unexplored area even in other well-known electrode materials. The discovery of a new olivine type would greatly attract broad readership among researchers in the energy and materials science fields, and it is most likely to reinforce the position of $LiFePO_4$-based cathodes as a material of choice for practical applications.

a Department of Materials Science and Engineering and Research Institute of Advanced Materials (RIAM), Seoul National University, 1 Gwanak-ro, Gwanak-gu, Seoul 151-742, Republic of Korea. E-mail: matlgen1@snu.ac.kr

b Center for Nanoparticle Research at Institute for Basic Science (IBS), Seoul National University, 1 Gwanak-ro, Gwanak-gu, Seoul, Republic of Korea

c Korea Atomic Energy Research Institute (KAERI), Daedeok-daero 989 Beon-Gil, Yuseong-gu, Daejeon, Republic of Korea

d Energy Lab, Material Research Center, Samsung Advanced Institute of Technology, Samsung Electronics Co., Ltd., 130 Samsung-ro, Yeongtong-gu, Suwon-si, Gyeonggi-do 16678, Republic of Korea

e Department of Chemical Engineering, Kangwon National University, Samcheok 245-711, Republic of Korea

f Beamline Department, Pohang Accelerator Laboratory, 80 Jigokro-127-beongil, Nam-gu, Pohang, Kyungbuk, Republic of Korea

g Department of Energy Science, Sungkyunkwan University, Suwon 440-746, 151-742, Republic of Korea

† Electronic supplementary information (ESI) available: Experimental details, neutron and X-ray structural analysis details, SEM images, ionic transport properties and DFT calculations on the defect formation energy of lithium-excess LFP. See DOI: 10.1039/c6ee01266c

‡ Present address: Lawrence Berkeley National Laboratory, Materials Science Division, Berkeley, CA 94720-8099, USA.

Introduction

The basic principle of modern rechargeable batteries relies on the reversible intercalation of guest ions in the electrode materials. The intercalation reaction is possible because numerous guest ions can diffuse in and out of the electrode crystal.[1] The diffusivity of the guest ions in the electrode, therefore, strongly affects the electrochemical properties, such as the power density, round-trip efficiency, and energy density. The crystal structure primarily determines the diffusivity of guest ions, providing specific diffusion paths. However, a deviation of the local atomic configuration around the guest ions also sensitively affects the ionic mobility.[2,3] For example, the presence of immobile defects in the diffusion paths, which may originate from impurities or anti-site defects, can significantly retard the mobility of ions. In particular, crystals with only one-dimensional diffusion pathways are susceptible to the presence of defects that may significantly impede Li-ion diffusion. In this respect, careful selection of the synthesis route or post-treatment of the electrode materials is often required to control the defect concentration.[4–6]

LFP has been intensely studied for the last two decades as a practically important cathode material for lithium rechargeable batteries and as a model system for thermodynamic and kinetic studies of lithium intercalation.[7–14] In the ideal case, LFP can deliver a specific capacity of 169 mA h g^{-1} via relatively fast lithium diffusion through a channel along the [010] direction of the crystal structure ($Pnma$).[13,15,16] However, in practice, approximately 5% Li–Fe cation site exchange (Li_{Fe}–Fe_{Li} anti-site defects) typically occurs, depending on the synthetic routes, which results in immobile Fe ions in the lithium diffusion channel.[3,17–22] Malik et al. demonstrated that the presence of 0.1% Li_{Fe}–Fe_{Li} anti-site defects in a micron-sized LFP particle statistically reduced its energy density to almost half of the original value[5,17] and decreased the lithium ionic conductivity by two or three orders of magnitude.[17] In this respect, many researchers have attempted to minimize Fe_{Li} anti-site defects from various synthetic routes.[5,17,23–25] Among these researchers, the Whittingham group succeeded in systematically analyzing Li_{Fe}–Fe_{Li} anti-site defects in LFP by controlling various synthetic conditions such as the hydrothermal methods and demonstrated that LFPs with high Li_{Fe}–Fe_{Li} anti-site contents suffer from inferior electrochemical performances.[20,22] Also, Hoang and Johannes investigated various point defects in LFP, calculating that the formation energy of the Fe_{Li}^+ defect is the highest among various defects under possible lithium-excess environments, i.e. $LiFePO_4$, $Li_3Fe_2(PO_4)_3$ and Li_3PO_4 equilibrium states.[26] The Masquelier group attempted to synthesize a highly defective LFP powder through a modified synthetic procedure, showing unexpected electrochemical behaviors. They revealed that a high concentration of defects could provide alternative lithium ion diffusion paths offering stable electrochemical performance based on distinct reaction mechanisms.[27–29] Although the nano-sizing of LFP is an indirect approach to reducing the effect of immobile Fe_{Li} defects because of the shortened diffusion length, nano-synthesis leads to other problems, such as reducing the tap density of the electrode,[23] generating more surface defects accompanying side reactions because of the large surface area,[30,31] and creating additional cost problems in synthesis and electrode fabrication.[32]

Incorporating additional charge-carrying guest ions in a crystal structure sometimes leads to unexpected results in their electrochemical properties,[33,34] which was recently demonstrated in layered-type lithium transition metal oxides. Armstrong et al. demonstrated that a slight excess of lithium ($x = \sim 3\%$) in $Li_{1+x}V_{1-x}O_2$ could switch on lithium-ion intercalation, delivering a higher theoretical specific capacity and volumetric energy density than graphite, whereas pristine $LiVO_2$ exhibits no evidence of intercalation into its structure.[33] In addition, lithium-excess derivatives of $Li(Ni,Co,Mn,Ru,Sn)O_2$ layered-type electrode materials, i.e., $Li_{1+x}(Ni,Co,Mn,Ru,Sn)_{1-x}O_2$, exhibit distinctive electrochemical responses during battery cycling, triggering oxygen redox reactions and delivering extra capacity beyond the expected value for the pristine materials.[35–40] Furthermore, recently, Lee et al. revealed that even fully disordered lithium transition metal oxides (100% anti-site ratio in the layered structure) can utilize the de/intercalation of almost all the lithium in the structure if a sufficient amount of excess lithium is present in the structure to provide a percolation path for lithium diffusion.[41] Also, earlier attempts on synthesizing $Li_{1+x}FePO_4$ ($x < 0.03$) exhibited better electrochemical properties than pristine $LiFePO_4$.[42,43] This series of new findings in lithium-excess layered electrode materials naturally motivated us to examine the strategy of lithium excessiveness in the olivine with $Li_{1+x}Fe_{1-x}PO_4$ compositions, which is an important electrode material and a class of crystals that could be more vulnerable to lithium kinetics because of the restricted diffusion path.

Based on this simple question, we attempted to adapt the lithium-excess concept to LFP ($Li_{1+x}Fe_{1-x}PO_4$) and successfully synthesize a lithium-excess phase by carefully controlling the synthetic conditions (see Fig. S1 in the ESI† for details). Structural analysis revealed that some Fe octahedral sites substitute with some Li ions. And, surprisingly, it is observed that the Li_{Fe}–Fe_{Li} anti-site defect concentration is remarkably decreased from Li ion diffusion channels in lithium-excess olivine. The near-zero Li_{Fe}–Fe_{Li} anti-site phenomenon is confirmed by DFT calculations and it is attributed to the fact that lithium-excess environments destabilized the formation of Fe_{Li}-related defects. Moreover, the lithium-excess local configurations could open new alternative diffusion paths through the [101] direction, lower the spinodal decomposition barrier and induce a significantly reduced memory effect in olivine cathode electrodes. Our results suggest an easy and cost-effective way toward developing a fast charge/discharge behavior of olivine cathode electrodes.

Results and discussion

Structural characterization of lithium-excess olivine

First, LFPs containing various lithium-excess compositions (0, 2.5, 5, 7.5, and 10%) were synthesized using solid-state methods at 600 °C in an Ar atmosphere to determine how much excess lithium could be incorporated into the olivine structure.
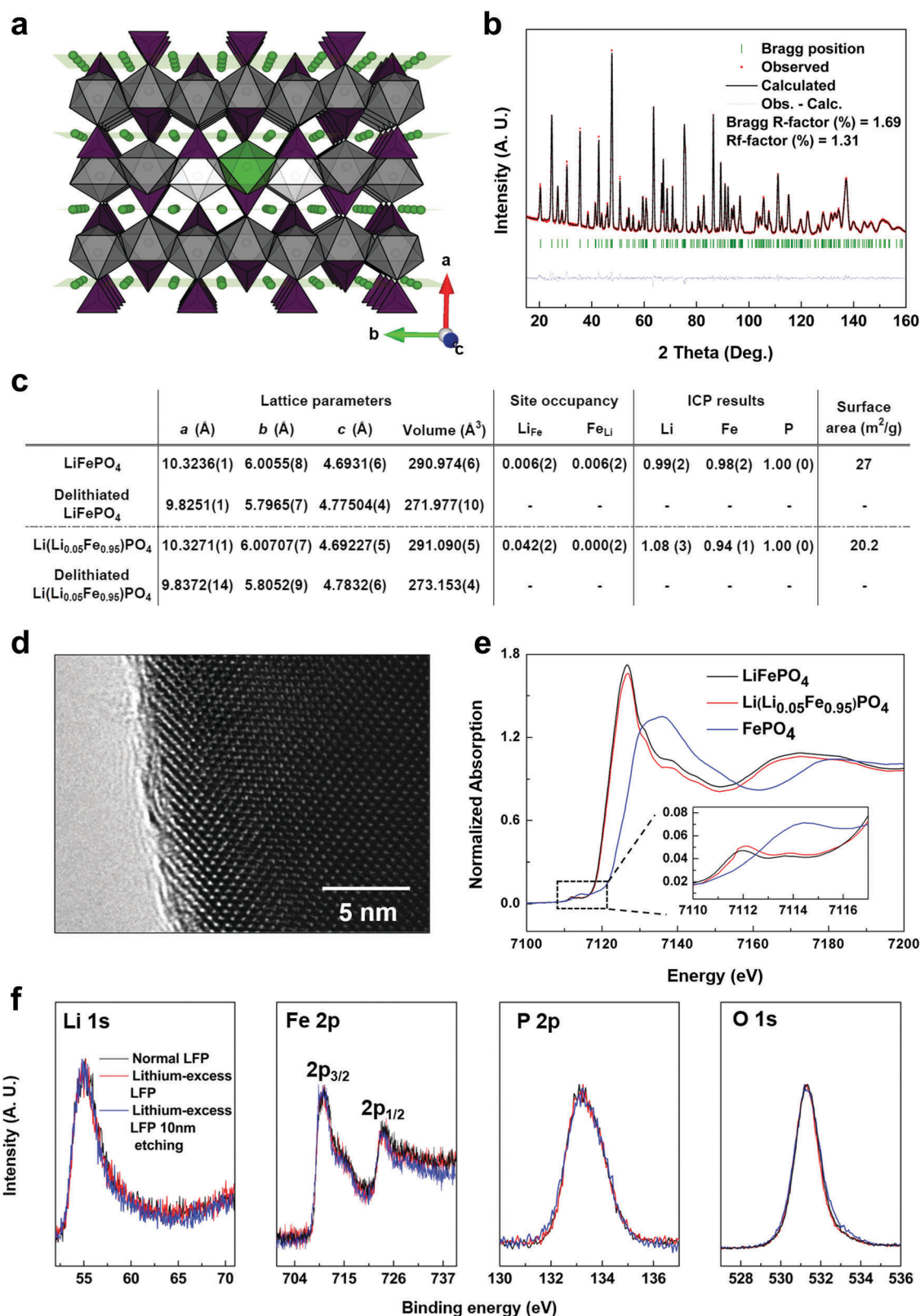
Although less than 5% lithium-excess LFP compositions result in a pure olivine phase without any crystalline impurities, compositions containing more than 7.5% excess lithium begin to develop a second phase corresponding to $Li_3Fe_2(PO4)_3$, as observed in the X-ray diffraction (XRD) patterns in Fig. S1 (ESI†). To verify the presence of additional lithium in the LFP crystal, a more detailed analysis was conducted using both high-resolution synchrotron XRD and neutron diffraction (ND), and the results were compared with those for normal LFP. Neutron analysis is necessary to trace the lithium occupancy in the crystal because of its low scattering with X-rays.[44] Fig. 1(b) presents the ND pattern of 5% lithium-excess LFP along with a calculated pattern using the olivine structure model, which shows low Bragg R-factors, indicating the reliability of the structural refinements. Detailed structural information from the refinements is provided in Fig. S2(a–c) (ESI†). In addition, as a reference, an ND pattern of the normal LFP along with the results of the refinement is presented in Fig. S2(d–f) (ESI†). Note that the 5% lithium-excess targeted LFP contains 4.2(2)% lithium in Fe octahedral sites (Li_{Fe}), and all the lithium sites are occupied solely by lithium (Li_{Li}) according to the neutron refinements in Fig. 1(c). On the other hand, the normal LFP contains ~0.6(2)% Li_{Fe}–Fe_{Li} anti-site defects according to the refinements under identical conditions, which agrees well with previously reported values of Li_{Fe}–Fe_{Li} anti-site defects in conventional LFPs.[15,16] The refinements of two samples using high-resolution XRD reproduced the same result for the two samples, as demonstrated in Fig. S3 (ESI†). The systematic modeling of the relative intensities of the XRD peaks as a function of the excess amount of lithium also agrees with the ND results given in Fig. S4 (ESI†). For a better comparison of the two samples, a few physical properties are tabulated in Fig. 1(c). The compositional analysis of two samples using inductively coupled plasma (ICP) supported the presence of an extra amount of lithium for the lithium-excess LFP phase, revealing a Li:Fe:P ratio of 1.08(3):0.94(1):1.00(0) and 0.99(2):0.98(2):1.00(0) for the lithium-excess and normal LFPs, respectively. The surface area is comparable for both samples but is slightly smaller for the lithium-excess LFP according to the Brunauer–Emmett–Teller (BET) measurements. The scanning electron microscopy (SEM) images in Fig. S5 (ESI†) show that the particle size of the lithium-excess LFP is slightly larger (~150 nm) than that of the normal LFP (~100 nm).

The excess amount of lithium in LFP leads to a slightly higher oxidation state of the transition metal (Fe) in the sample to maintain charge neutrality based on the substitution of the monovalent Li^+ for divalent Fe^{2+} ($Li(Li_{0.05}^+Fe_{0.95}^{+2.053})PO_4$). The X-ray absorption near edge structure (XANES) analysis in Fig. 1(e) compares the oxidation states of Fe in three samples of $Li(Li_{0.05}Fe_{0.95})PO_4$, $LiFe^{+2}PO_4$, and $Fe^{+3}PO_4$. Although the quantitative determination of the Fe valence in the lithium-excess LFP was not trivial, it was clear that the Fe pre-edge spectra of the lithium-excess LFP (7112.19 eV) are positioned between those of $LiFePO_4$ (7111.85 eV) and $FePO_4$ (7114.35 eV), indicative of a Fe valence higher than +2.[45,46] Furthermore, a small increase of the pre-edge peak intensity is observed at the $Li(Li_{0.05}Fe_{0.95})PO_4$, implying that the lithium-excess LFP contains

a more distorted Fe–O octahedron than that of the normal LFP.[46] The higher oxidation state and distorted local structure of the Fe ion of the sample also serve as indirect evidence of the excess lithium present in the structure.

Even though the crystallographic information and compositional analysis indicate the presence of the excess lithium in the olivine, the possibility of the formation of an amorphous impurity phase remains. According to previous reports, the synthesis of LFP using a slightly off-stoichiometric amount of precursors can result in LFP coated with a highly conductive amorphous phase, enhancing the rate capability.[47–49] To identify any possible amorphous phase, we conducted surface analysis of the lithium-excess LFP using high-resolution transmission electron microscopy (HR-TEM), X-ray photoelectron spectroscopy (XPS), and Fourier-transform infrared spectroscopy (FT-IR). The HR-TEM images (Fig. 1(d) and Fig. S8, ESI†) reveal the high crystallinity of the lithium-excess LFP both at the surface and in the bulk without an amorphous phase on the surface. In addition, the XPS and FT-IR results show no difference between the surface and bulk of the lithium-excess LFP. Both the pristine and 10 nm surface-deep-etched lithium-excess LFPs exhibited identical XPS and FT-IR profiles, as observed in Fig. 1(f) and Fig. S9 (ESI†), respectively, implying no traceable amount of the amorphous phase on the lithium-excess LFP surface.

Further confirmation of the excess lithium in the LFP could be obtained from the ^6Li-NMR measurement using ^6Li-labeled samples. Fig. 2(a) presents the NMR spectra of $^6LiFePO_4$ and $^6Li(^6Li_{0.05}Fe_{0.95})PO_4$. Except for the side bands marked with asterisks, a single Li signal is observed between 0 to −100 ppm for both samples. In the zoomed-in view in Fig. 2(b), the normal LFP shows a lithium signal at −49 ppm, which is in good agreement with previous reports.[50,51] However, a less-negative-shifted major NMR signal is observed for the lithium-excess LFP at −18 ppm. In addition, the asymmetric nature of the major signal strongly suggests that a small positive-shifted minor peak (+47 ppm) is present based on the spectral deconvolution. In the olivine $LiFePO_4$ crystal, the Li_{Li} (octahedral, M1 site) is coordinated with six oxygen atoms, which also coordinate with six different iron atoms (octahedral, M2 site), as illustrated in Fig. 2(c). The Li–O–Fe bonds around Li_{Li} result in near-90° Li–O–Fe angle contacts, inducing a strong paramagnetic interaction (marked by the red dashed line in Fig. 2(c)), and 120°-angle contacts, inducing a relatively weak paramagnetic interaction (marked by the blue dashed line in Fig. 2(c)). The major NMR peak at −49 ppm in normal LFP or −18 ppm in lithium-excess LFP primarily originates from the strong near-90° Li–O–Fe interaction resulting from the geometry-dependent delocalization of the unpaired electron spin density of Fe^{2+}.[50,51] However, the less-negative shift of the major peak for lithium-excess LFP (−18 ppm) is most likely due to the slightly higher average oxidation state of Fe ions around Li_{Li}. Previous NMR reports on $LiFePO_4$, $Li_{0.6}FePO_4$, and $Li_{0.54}FePO_4$ indicated that the major NMR peak gradually shifts to higher frequency (less negative values) with decreasing lithium content and increasing Fe^{3+} content in the olivine, which is consistent with our results.[50,52–54] The excess lithium residing in the Fe site (Li_{Fe} anti-site) results in an

2904 | Energy Environ. Sci., 2016, 9, 2902–2915

This journal is © The Royal Society of Chemistry 2016

Fig. 1 (a) Schematic picture of crystalline lithium-excess LFP. Green: Li atoms, purple: PO_4 tetrahedral unit, gray: $Fe^{2+}O_6$ octahedral unit. (b) Rietveld refinement of the neutron diffraction pattern of lithium-excess LFP. Detailed crystal structure information is provided in Fig. S2 and S3 (ESI†). (c) Lattice parameters, M1 and M2 site occupancy, ICP results and surface area of lithium-excess and normal LFPs. (d) TEM image of the lithium-excess LFP surface. (e) Fe XANES measurements for three samples of lithium-excess LFP, normal LFP and normal FP (delithiated LFP). The lithium-excess LFP olivine shows a slightly higher Fe oxidation state than that in the normal LFP as shown in the inset figure for zoomed-in pre-edge range. (f) Surface analysis of 5% lithium-excess LFP (red line) and normal LFP. (black line) 10 nm etched surface of lithium-excess LFP is marked by blue lines (left to right, Li 1s, Fe 2p, P 2p and O 1s XPS).
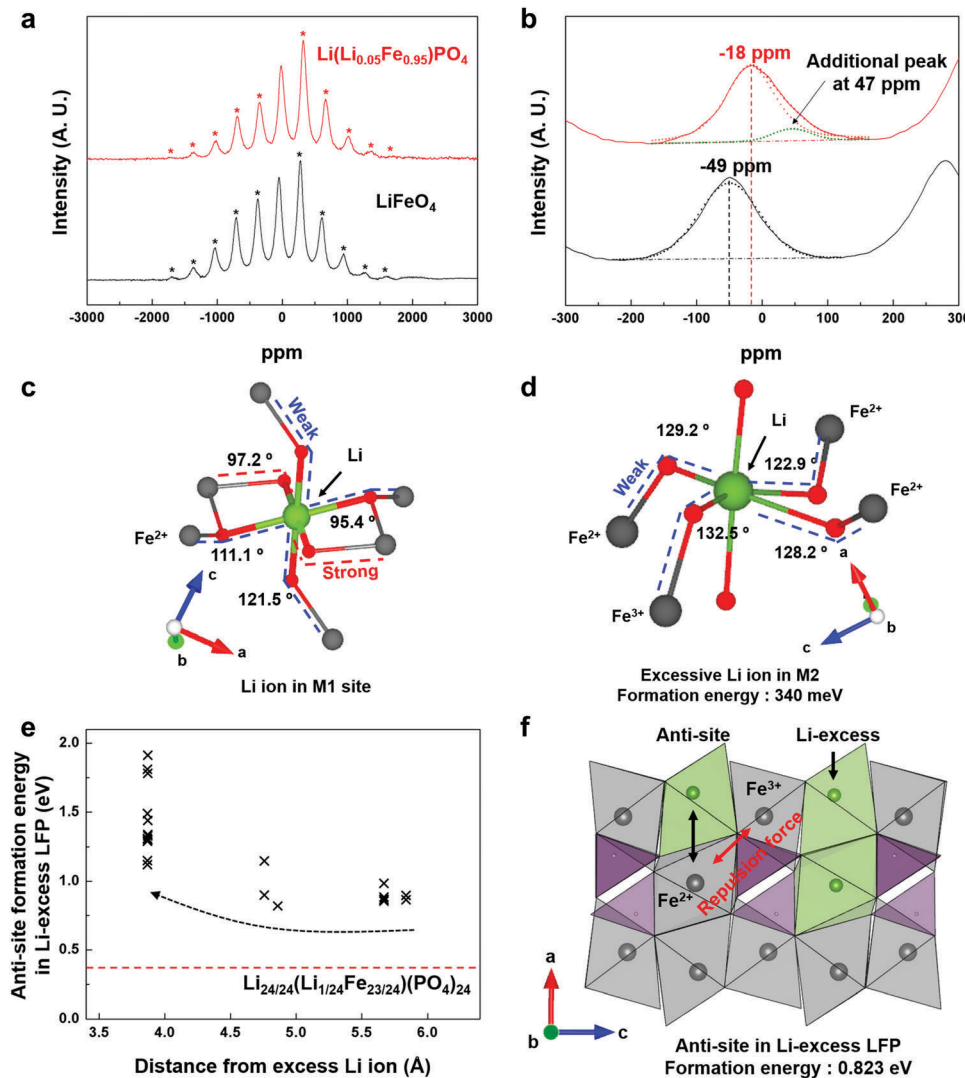
Fig. 2 (a) ^{6}Li NMR resonance of lithium-excess LFP (red) and normal LFP (black) with side bands (asterisk). (b) Spectral deconvolution of ^{6}Li NMR peaks. The normal LFP contains single resonance at −49 ppm, and the lithium-excess LFP contains two resonances at −18 and +47 ppm. (c) Local atomic configuration around Li ions in the M1 site in normal LFP and (d) excess Li ions in M2 in lithium-excess LFP calculated by the DFT method. The red and blue dashed lines indicate strong and weak paramagnetic interactions between Li and Fe ions, respectively. (e) Li_{Fe}–Fe_{Li} anti-site defect formation energies in lithium-excess LFP as a function of distance from Li_{Fe}. The red dashed line indicates the lithium-excess formation energy (340 meV). (f) The most stable anti-site configuration in lithium-excess LFP.

additional minor peak at +47 ppm in the lithium-excess LFP. According to the previous NMR report on the normal LFP that contains a significant amount of Li_{Fe}–Fe_{Li} anti-site defects, the lithium in Fe sites (M2) with a similar environment to the Li_{Fe} ions in our lithium-excess LFP exhibited a positive NMR peak shift at +75 ppm.[52] Our density functional theory (DFT) calculations (Fig. 2(d) and Fig. S10, ESI†) regarding the local atomic configuration around the excess lithium revealed that the four Fe ions are bonded with the Li_{Fe} ion through oxygen atoms via a near-120° Li–O–Fe angle, whose configuration leads to the comparatively weak paramagnetic shift. This unique environment of the Li_{Fe} ions generates a relatively lower paramagnetic shift, yielding a positive chemical shift at +47 ppm. Also, we could confirm the local structure change of lithium-excess LFP by Fe K-edge extended X-ray absorption fine structure (EXAFS) analysis (Fig. S11, ESI†).

To understand the thermodynamic feasibility of the lithium-excess LFP phase, we attempted to estimate its relative formation energy against the segregation into thermodynamically stable phases of $LiFePO_4$, Li_3PO_4, and $Li_3Fe_2(PO_4)_3$ as follows:

$$Li_{1+x}Fe_{1-x}PO_4 \ (x \leq 0.5) \rightarrow (1-2x)LiFePO_4 + 0.5xLi_3PO_4 \\ + 0.5xLi_3Fe_2(PO_4)_3.$$
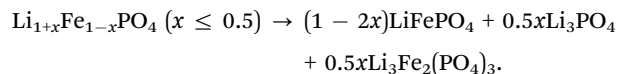
Based on this equation, we calculated the formation energy of 5% lithium-excess LFP using the $Li_{24/24}(Li_{1/24}Fe_{23/24})(PO_4)_{24}$ model (168 atoms in a unit cell) at zero temperature excluding the entropic effect. The formation energy for one excess lithium (Li_{Fe}) was observed to be approximately 340 meV per event, indicating that the excess lithium ions formed an 'anti-site defect' state in their structure. Considering the relationship

2906 | Energy Environ. Sci., 2016, 9, 2902–2915

This journal is © The Royal Society of Chemistry 2016

between the defect formation energy and its concentration, the comparison of various defect formation energies would provide a rough idea of the feasibility of the excess lithium 'defects' in the olivine, particularly for defects in an olivine framework.[2] It is noteworthy that the formation energy of Li_{Fe}–Fe_{Li} anti-site defects in typical olivine $LiFePO_4$ is approximately 420 meV per event, and depending on the synthetic routes, olivine LFPs with $\sim$5% Li_{Fe}–Fe_{Li} anti-site defect concentration can be easily synthesized.[5] Thus, the synthesis of the olivine LFP with $\sim$5% excess lithium, which requires $\sim$340 meV defect formation energy, may be plausible. However, as is the case for the typical olivine LFP, which generally shows low defect concentrations with higher temperature post heat treatments,[5,55] we also observed that the 5% lithium-excess LFP was not stable under such conditions. For example, at the temperature above 700 °C where normal LFP could be synthesized, lithium-excess LFP decomposed into normal LFP, $Li_3Fe_2(PO_4)_3$ and Li_3PO_4 phases. Similarly, a sintering time longer than 20 hours gave rise to the decomposition of lithium-excess LFP into normal LFP and an impurity phase (see ESI† and Fig. S12 for a detailed synthetic process). Thus, a very narrow range of heat treatment temperature and duration hours was allowed for the synthesis of a lithium-excess concentration in LFP. It indicates that the lithium-excess concentration in the LFP crystal structure is a kinetically trapped meta-stable system caused by the relatively low temperature and sintering time during the synthesis process.
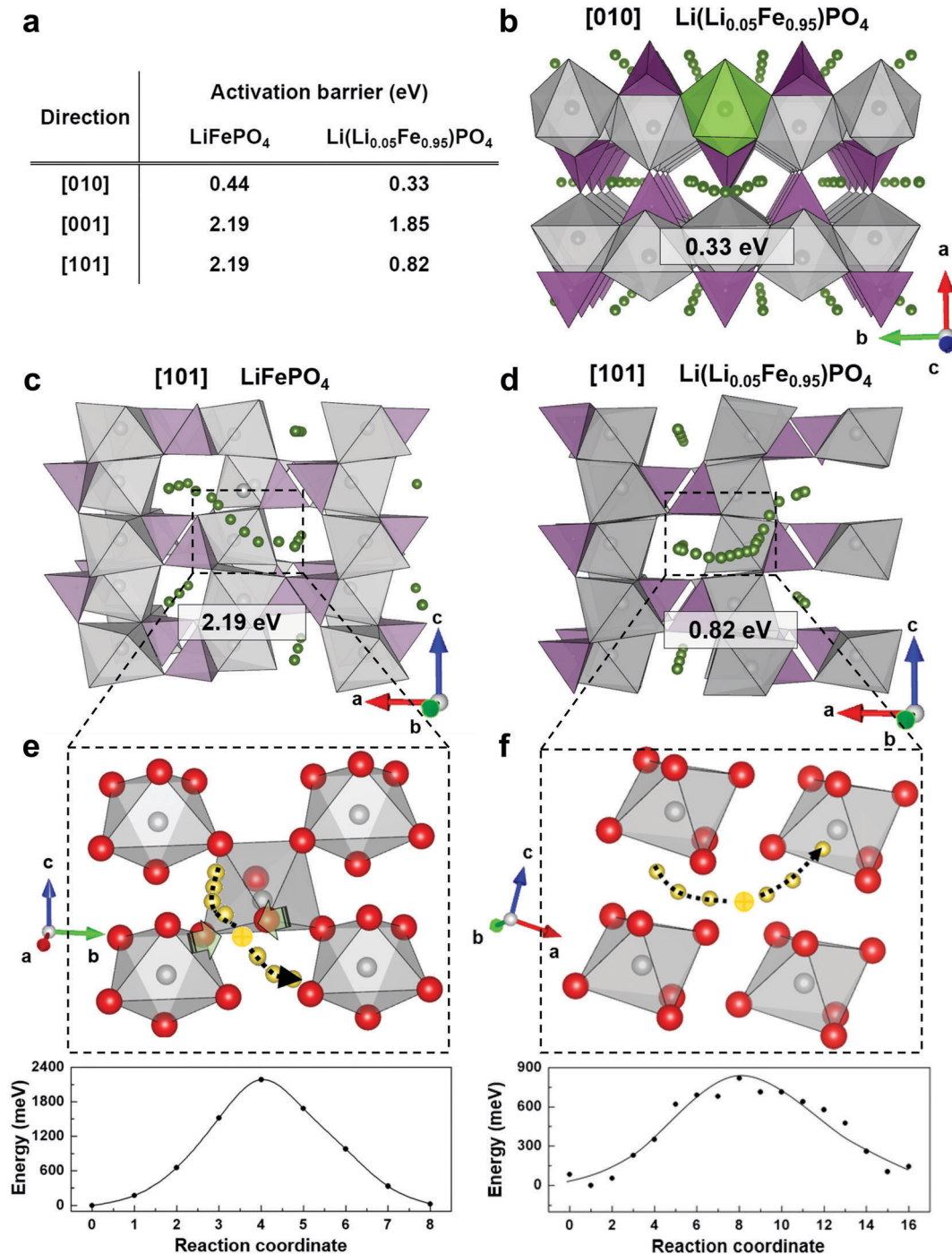
Origin of decreasing Li_{Fe}–Fe_{Li} defect concentration

Given the structural analysis of lithium-excess LFP, most notably, it contains near-zero Fe_{Li} anti-site defects in the M1 sites. A reduction of the number of transition metal defects in lithium sites was also similarly observed in lithium-excess $Li(Li_x,(Ni,Mn)_{1-x})O_2$ ($x > \sim 0.2$) with less Li/Ni site disorder up to 2%,[56] however, the complete disappearance of Fe ions in the lithium diffusion channel with only 5% excess lithium is quite remarkable. To further understand the role of the excess lithium present in the structure in reducing the concentration of Fe_{Li} defects, we calculated the defect formation energies in local atomic configuration containing Fe_{Li} defects around excess lithium (Li_{Fe}) using DFT calculations. (Note that the Li_{Fe}–Fe_{Li} anti-site defect has the lowest formation energy among the possible Fe_{Li}-related defects in LFP in a lithium-excess environment according to previous theoretical work,[26] therefore, we only considered the local lithium-excess configuration effect on Li_{Fe}–Fe_{Li} anti-site defects in this calculation.) In this calculation, we considered 17 different Li_{Fe}–Fe_{Li} anti-site defect configurations around the excess lithium up to the second-nearest transition metal neighbors along each axis (Fig. S13, ESI,† shows detailed atomic configurations). All defect formation energies of the 17 different configurations are shown as a function of the distance from excess Li_{Fe} ions in Fig. 2(e). It is observed that the Li_{Fe}–Fe_{Li} anti-site energy generally increases as it approaches the excess lithium, indicating that the presence of excess lithium energetically disfavors the formation of a Li_{Fe}–Fe_{Li} anti-site defect near itself. We also observed that even the lowest defect formation energy (Fig. 2(f)) was as high as 0.823 eV, which is 2 times larger

than the typical Li_{Fe}–Fe_{Li} anti-site formation energy (0.42 eV, see Fig. S14, ESI†) observed in normal LFPs.[3] Because the defect formation is inversely proportional to the exponential value of the formation energy, an increase in the formation energy by $\sim$0.4 eV would reduce the probability of Li_{Fe}–Fe_{Li} anti-site formation near the excess lithium (Li_{Fe}) by 7 orders of magnitude at room temperature. This remarkable reduction arises from the unfavorable electrostatic interaction among Fe ions around the excess lithium (Li_{Fe}), as shown in Fig. 2(f). When the Li_{Fe}–Fe_{Li} anti-site is introduced near the excess lithium (Li_{Fe}), the neighboring Fe ion becomes oxidized to Fe^{3+} in the locally lithium-rich region. In addition, under this condition, the site-exchanged Fe^{2+} ion (Fe_{Li}) suffers from a stronger repulsion force from the neighboring Fe^{3+} ion (Fig. 2(f), red arrow), which significantly increases the formation energy of the Fe_{Li} anti-site. In this respect, when the Li_{Fe}–Fe_{Li} anti-site configuration becomes close to the lithium-excess configuration, the site-exchanged Fe^{2+} ion has a strong repulsion force towards Fe^{3+} ions which leads to an increase in the anti-site defect formation energy as shown in Fig. 2(e). Considering that the one excess lithium event affects at least 17 neighboring Fe ion sites among the second-nearest neighbors we considered, approximately 4% excess lithium would result in all the Fe ion sites being affected if the excess lithium ions were homogeneously distributed in the olivine crystal. Thus, the overall Li_{Fe}–Fe_{Li} anti-site concentration in the lithium-excess LFP would be 1.2×10^{-7} times less than that in normal LFP at room temperature. This finding implies that the excess lithium in the olivine reduces the Li_{Fe}–Fe_{Li} anti-site by energetically disfavoring the formation of anti-sites near the lithium-excess, suggesting that this approach could be effective in producing a near-zero Li_{Fe}–Fe_{Li} anti-site olivine. Our results also partly agree with a previous theoretical work by Hoang and Johannes. They investigated the LFP defect profile under various atomic chemical potential spaces, calculating that undesired Fe_{Li}-related defect formation energy increases in a lithium-excess environment.[26] The understanding of the decrease in Fe_{Li} concentration in the lithium-excess LFP can also be aided from the overall pictures of the defect profile of the LFP in their work.

Possibility of alternative diffusion paths

The occupancy of excess lithium in the Fe site can open up a new lithium diffusion pathway by connecting the nearby lithium channels. It is well known that the olivine crystal has only one diffusion channel along the [010] direction with a low activation barrier ($\sim$0.44 eV), whereas lithium diffusion across the channels in other directions such as [101] or [001] requires too high of an activation barrier because of the strong electrostatic repulsion from the Fe and insufficient space for lithium hopping, as listed in Fig. 3(a).[57,58] The replacement of the high-valent Fe ions by lithium ions reduces the electrostatic repulsion, thus facilitating lithium hopping around the lithium (Li_{Fe}), as observed in the reduction of the activation barriers along [001] and [010]. Also, the lowered lithium ion diffusion activation energies could be confirmed by electrochemical impedance spectroscopy (EIS) measurement (see Fig. S15, ESI†). It is noteworthy that the excess

This journal is © The Royal Society of Chemistry 2016

Energy Environ. Sci., 2016, **9**, 2902–2915 | **2907**

Fig. 3 (a) Activation barriers for lithium ion hopping for normal and lithium-excess LFPs. The schematics of Li ion diffusion along the (b) [010] direction in lithium-excess LFP, (c) [101] direction in normal LFP and (d) [101] direction in lithium-excess LFP with activation energies. (Green: Li atoms, purple: PO_4 tetrahedral unit, dark gray: FeO_6 octahedral unit, yellow: vacancy.) The lithium-excess LFP shows lower activation energies than normal LFP in both the [010] and [010] directions. (e and f) A close view of vacancy diffusion along with the energy profiles. (Vacancy in the highest energy state marked by bright yellow. Red: O, gray: Fe).

lithium in the Fe site can also be mobile and may diffuse into the nearby lithium channel along [101], participating in the overall diffusion process in the crystal. Our DFT calculations reveal that the presence of lithium in the Fe site opens up a new alternative diffusion path along the [101] direction with a significantly reduced activation barrier of ~0.82 eV (Fig. 3(d))

compared with more than 2 eV for normal LFPs (Fig. 3(c)) along the same direction.[59] The calculated activation barrier is also similar to the value reported by Dathar *et al.* along the [101] diffusion channel containing Li_{Fe}–Fe_{Li} anti-site defects.[60] Fig. 3(e) and (f) present a schematic illustration of lithium vacancy hopping along the [101] direction and the corresponding energy profile

2908 | *Energy Environ. Sci.*, 2016, **9**, 2902–2915

This journal is © The Royal Society of Chemistry 2016

for normal and lithium-excess LFPs. In the normal LFP, the lithium-ion hopping along the [101] direction is under severe electrostatic repulsion from the nearby corner-sharing Fe ions, and the lithium ion is forced to pass through the oxygen dumbbell, as shown in Fig. 3(e). The narrow space between the two oxygens ($\sim$3.05 Å) disfavors the lithium hopping, resulting in an activation barrier of more than 2 eV. In the lithium-excess LFP, however, the corner-sharing Fe is replaced with lithium, which also participates in the diffusion. Thus, the diffusing lithium ion no longer needs to bypass the high-valent Fe and can hop through the space provided by Li_{Fe} (Fig. 3(f)). Since the lithium occupation in the Li_{Fe} site is more favorable than in the Li_{Li} site (Fig. S16, ESI†), lithium-ion hopping along the [101] direction in lithium-excess LFPs could be described by a two-step process; (1) migration of Li_{Fe} to vacant Li_{Li} (rate-limiting step) and (2) consecutive diffusion of Li_{Li} to vacant Li_{Fe} (Fig. S16(b), ESI†). Compared with normal LFP, where the lithium ion squeezes into the narrow oxygen dumbbell, the new intermediate state offered by the Li_{Fe} site provides sufficient space, thus lowering the activation barrier for hopping. Also, the additional diffusion paths in lithium-excess LFP are experimentally visualized by the maximum entropy method (MEM) using high temperature neutron diffraction, which strongly supports our calculation results on the [101] diffusion path (see Fig. S17, ESI†).

The activation barrier of $\sim$0.82 eV is slightly higher than that observed for fast lithium pathways but is comparable to that of diffusion paths observed for $NaFeSO_4F$[61] and $LiMnPO_4$,[62] implying feasible lithium diffusion along the new path. The [101] route may not be a main diffusion path during fast charge/discharge cycling at room temperature considering the higher activation energy compared with that of the [010] diffusion path and a relatively low concentration of lithium-excess, but would support the main [010] diffusion channel as an alternative route, particularly in the presence of immobile impurities in the [010] channel. It is noteworthy that a similar phenomenon was observed in rock-salt-type lithium-excess $Li_{1.211}Mo_{0.467}Cr_{0.3}O_2$, which exhibited remarkably enhanced ionic conductivity and capacity with the introduction of an excess amount of lithium, implying that the 'excess-lithium strategy' can be used as a general method to open multiple new lithium diffusion paths in solid-state lithium ionic conductors.[41]

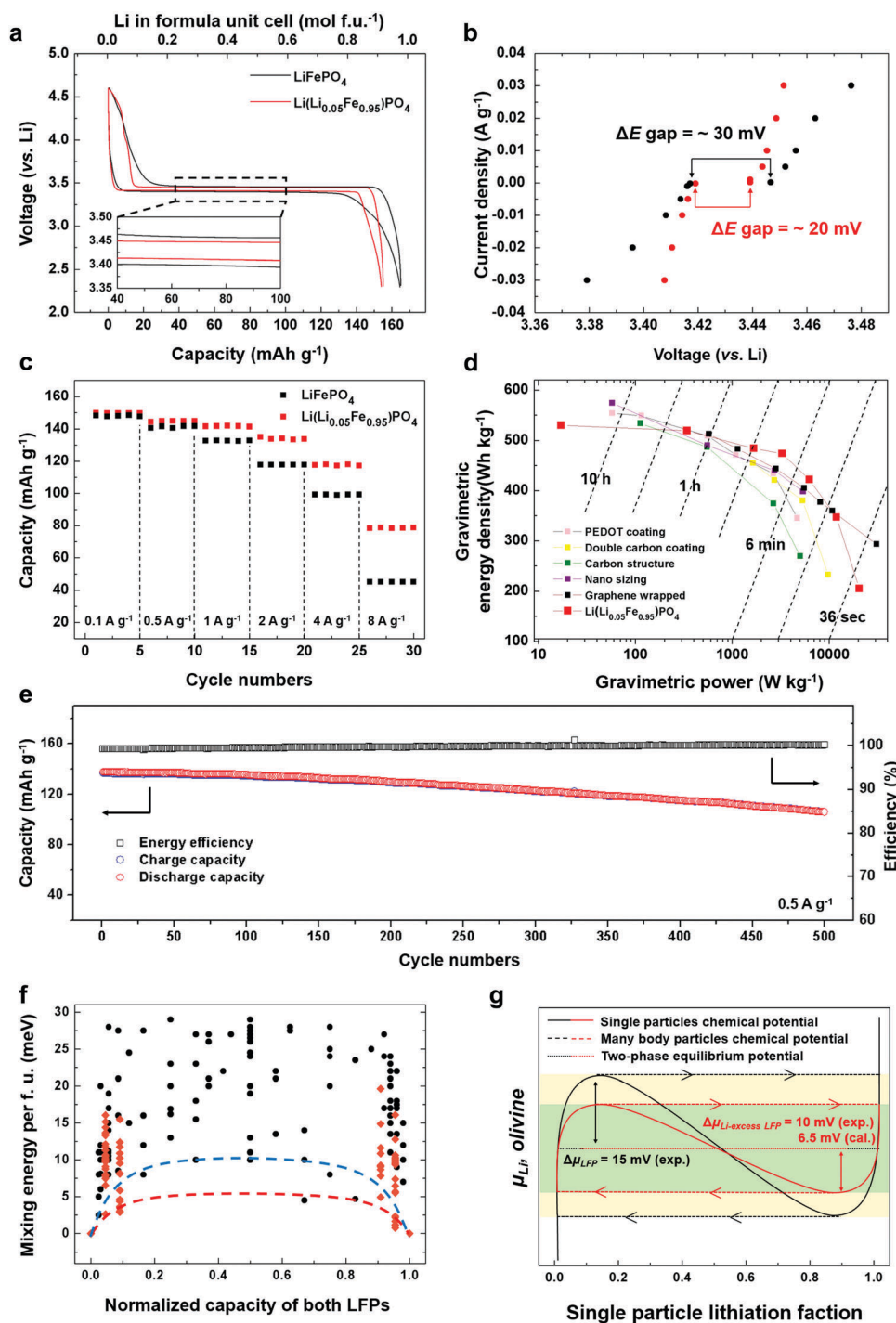### Electrochemical performance of lithium-excess LFP

The electrochemical properties of lithium-excess LFP were investigated using a Li metal counter electrode in a 2032 coin-type cell. Fig. 4(a) presents the galvanostatic electrochemical profiles of lithium-excess LFP compared with that of normal LFP at a 10 mA g^{-1} current rate (red: lithium-excess LFP, black: normal LFP). The lithium-excess LFP electrode delivers a slightly lower capacity of $\sim$157 mA h g^{-1} compared with the normal LFP, $\sim$166 mA g^{-1}, which is due to the higher oxidation state of Fe and the smaller number of available $Fe^{2+/3+}$ redox couples in $Li^{1+}(Li^{1+}_{0.05}[Fe^{2+}_{0.90}Fe^{3+}_{0.05}])PO_4$. In addition, the voltage plateau region of the lithium-excess LFP ($\sim$130 mA h g^{-1}) is slightly wider than that of the normal LFP ($\sim$115 mA h g^{-1}). We infer that the different two-phase region of lithium-excess LFP is

attributed to larger particle size and reduced lattice misfit as described in Fig. 1(c).[63,64] Nevertheless, it is notable that a lower polarization gap between charge and discharge was observed for lithium-excess LFP compared with normal LFP under the same electrochemical conditions. The smaller polarization was consistently observed with varying current densities from 30 mA g^{-1} to 0.17 mA g^{-1}, corresponding to a C/1000 rate of LFP, as shown in Fig. 4(b). With the extrapolation of the curve toward zero current, the minimum values of the hysteresis gaps reach 20 mV and 30 mV for lithium-excess and normal LFP, respectively. As the near-zero-current polarization of LFP is related to the delithiation mechanism of single-particle LFP and has been regarded as a thermodynamic property, the different values of the two LFPs imply distinguishable delithiation behaviors, as will be discussed in further detail. Additional experiments and discussion regarding the zero-current polarization is provided in Fig. S18, ESI.†

The rate capabilities of lithium-excess LFP were measured at various current rates as shown in Fig. 4(c). (The charge/discharge profiles are provided in Fig. S19, ESI.†) The lithium-excess LFP electrode exhibited a notably improved rate capability compared with that of the normal LFP even though the particle size of lithium-excess LFP is slightly larger, as previously illustrated. Lithium-excess LFP delivers a discharge capacity of 78 mA h g^{-1} at a current density of 8 A g^{-1}, which is equivalent to approximately 50C (Fig. 4(c)). Compared with normal LFP electrodes, this value represents an approximately 2-times-higher capacity. The specific power density calculated at 8 A g^{-1} is approximately 20 kW kg^{-1}, which is comparable with other previously reported LFPs that have underwent surface chemical modification, nano-sizing processes or graphene composite LFPs, as shown in Fig. 4(d).[65–69] In addition, the lithium-excess LFP electrode still exhibits higher rate capability than that of the normal LFP at a lower temperature of 0 °C. The lithium-excess LFP delivers a discharge capacity of $\sim$66 mA h g^{-1} at a current density of 2 A g^{-1}, which is $\sim$30% higher than that of normal LFP ($\sim$49 mA h g^{-1}) at the same current density (see Fig. S20, ESI†). After 500 cycles at 0.5 A g^{-1}, the lithium-excess LFP still exhibited 82% retention of the initial capacity, maintaining a high charge/discharge efficiency as shown in Fig. 4(e). (The capacity retention of the normal LFP at the same current rate (0.5 A g^{-1}) and the XRD pattern comparisons on both LFPs before and after cycling are exhibited in Fig. S21, ESI.†)

Lowering the spinodal decomposition barrier

A single-particle solid–solution equilibrium model was recently proposed and is now widely accepted for LFP electrode systems.[7,8,70,71] According to the model, the free energy of small-size LFP particles is significantly modified by the interfacial and coherency energy, which comes as a positive energy penalty,[63] leading to the lithium chemical potential profile of LFP single-particles changing from a two-phase to single-phase-like feature. The collected behavior of single particles in the electrode containing numerous LFP particles is the origin of the thermodynamic hysteresis gap between the charge and discharge.[70,71] The lower hysteresis gap ($\sim$20 mV) compared with that of

This journal is © The Royal Society of Chemistry 2016

Energy Environ. Sci., 2016, **9**, 2902–2915 | **2909**

Fig. 4 (a) Charge/discharge curves of normal LFP (black) and lithium-excess LFP (red) at a current density of 10 mA g^{-1}. The inset figure exhibits magnified charge/discharge curves near the plateau region. The lithium-excess LFP shows lower polarization than normal LFP. (b) Hysteresis gap of normal LFP (black) and lithium-excess LFP (red) at various current densities. Zero-current hysteresis gap of normal and lithium-excess LFPs are obtained at around 30 mV and 20 mV, respectively. (c) Rate capability of lithium-excess LFP (red) and normal LFP (black). (d) Ragone plot of various surface or chemical modified LFPs. The lithium-excess LFP shows lower gravimetric energy density than other modified LFPs at a low current rate, however, improved energy and power density are exhibited at higher current rates. (Ref.: nano-sizing,[65] carbon structure,[66] double carbon coating,[67] PEDOT coating[68] and graphene/LFP composite.[69]) (e) Cycle life test of lithium-excess LFP with a current density 0.5 A g^{-1}. (Corresponding to 2.95 C of normal LFP.) The capacity after 500 cycles maintained 81.5% of the initial charge/discharge capacity. (f) Mixing free energy and atomic configuration of lithium-excess LFP (orange) and normal LFP (black, ref. 70, copyright 2011, Nature Publishing Group) as a function of lithium contents. Mixing energies of lithium-excess and normal LFP at zero-temperature. Black dots and blue line are taken from the work of Ceder et al.[70] The free energies were calculated by DFT calculations using 245 atoms. The dash line is a predicted curve of whole mixing free energy. (Lithium-excess LFP: orange, normal LFP: blue dash line.) (g) The single particle chemical potential of normal LFP (black) and lithium-excess LFP (red) as a function of the lithiation faction. The normal LFP and lithium-excess LFP contain ~15 mV and ~10 mV phase transition activation barriers, respectively.

2910 | Energy Environ. Sci., 2016, **9**, 2902–2915

This journal is © The Royal Society of Chemistry 2016

normal LFP ($\sim$30 mV) that we observed in Fig. 4(b) indicates that lithium-excess LFP is likely to possess a distinct single-particle characteristic. To understand this phenomenon in detail, we investigated the preference toward the single-phase-like behavior changes resulting from the presence of excess lithium in LFP by calculating the free energy of mixing using DFT methods, as shown in Fig. 4(f). For reference, the phase mixing energies of normal LFP were taken from the work of the Ceder group in ref. 70 (black dots) and plotted together with those of excess-lithium LFP (orange dots) as a function of the lithium content. Compared with the minimum mixing free energies of normal LFP at each lithium composition (blue line),[70] those of the lithium-excess LFP (red line, see Fig. S22, ESI† for detailed energy calculations and atomic configurations) lie well below, indicating that the lithium-excess LFP is energetically much closer to the single-phase energy over all the lithium compositions, i.e., it deviates less from the tie-line of the LFP two-phase reaction.[70] This relation between the energy and lithium content of Fig. 4(f) can be roughly converted into a plot with respect to the lithium chemical potential, as presented in Fig. 4(g). The figure presents a schematic energy profile of a single-particle electrode that undergoes a solid–solution for both cases of lithium-excess (red line) and normal (black line) LFPs. The spinodal energy per lithium to overcome for lithium-excess LFP ($\Delta\mu_{\text{Li-excess LFP}}$) was approximately 6.5 mV according to DFT calculations and $\sim$10 mV according to experiments. These values are only two-thirds of those of normal LFPs ($\Delta\mu_{\text{LFP}}$, $\sim$15 mV),[70,71] which implies that the energy to overcome is much less for the single-phase-like reaction in the case of lithium-excess LFP. According to the particle-to-particle intercalation model,[71] discrete one-by-one filling of many particles occurs, and the energy barrier for the single particle results in the voltage hysteresis between the charge and discharge plateau, as illustrated in Fig. 4(g). The smaller hysteresis gap in lithium-excess LFP derived from this figure agrees well with the results in Fig. 4(b). It is speculated that the lower phase-transition energy barrier for lithium-excess LFP stems from the defective nature of lithium in the Fe site (Li_{Fe}) that destabilizes the pristine phase and promotes the mixing as a "*phase mixing seed*". In addition, the reduced lattice misfit between lithium-excess LFP and delithiated lithium-excess LFP as listed in Fig. 1(c) is also believed to be affected on reducing the phase transition barrier.[7,71]

Reduced memory effect of lithium-excess LFP

Another aspect that we investigated for lithium-excess LFP was how the reduced energy barrier for the transition affects the (i) 'overshooting' of voltage during charge/discharge and (ii) the memory effect that has recently been reported for normal LFP.[7] T. Sasaki et al. demonstrated that the electrochemical profile of LFP exhibits an anomalous polarization increase depending on the relaxation time and is affected by the history of the cycling.[7] This increase was explained using a particle-by-particle charge/discharge model with non-uniform chemical potentials of LFP single particles after relaxation.[7] When the LFP electrode stops at certain charge or discharge states, the active LFP particles begin to separate into Li-rich and Li-poor particles. The active

particles not reaching the most stable state during relaxation do not show additional polarization, whereas those that have reached this state have to climb up the energy barrier again, inducing higher polarization.[7] We also observed an anomalous polarization increase after relaxation in the galvanostatic intermittent titration technique (GITT) compared with the constant current (CC) measurements for normal LFP, as observed in Fig. 5(a). Also, consistent with the observation of T. Sasaki et al., the memory effect is clearly observed for normal LFP after the memory writing cycle (Fig. 5(b)). However, it was noted that lithium-excess LFP exhibits a much smaller increase in the polarization after relaxation in the GITT, as observed in Fig. 5(c), and does not exhibit any detectable memory effect even after we applied the same memory writing cycle as that of the normal LFP electrode, as shown in Fig. 5(d).

Considering the memory effect model proposed by Sasaki et al., we could infer that the lithium-excess LFP particle has a different relaxation behavior from the normal LFP. To further compare the relaxation behavior and polarization increase of lithium-excess and normal LFP electrodes, we designed an additional experiment of rest-time-dependent partial GITT. Before performing the partial GITT, the open-circuit voltage (OCV) at 50% state of charge (SOC) was measured during relaxation after charge or discharge with a current rate of 10 mA g^{-1} as a function of time, as shown in Fig. 5(e). Although the OCV of normal LFP required more than 100 min to obtain a charge and discharge gap of 30 mV, the OCV gap of lithium-excess LFP was reduced to 10 mV in less than 20 min. This result indicates that the relaxation process occurs much faster for lithium-excess LFP, which is attributed to the higher degree of lithium diffusion in the lithium-excess LFP. For a qualitative comparison, measurement of the diffusion coefficients for the two LFPs was performed as illustrated in Fig. S23–S25 (ESI†), indicating that the lithium-excess LFP has one-order higher conductive properties than the normal LFP. The difference in the relaxation kinetics affects the behavior of the GITT experiment. Fig. 5(f) and (g) show the partial GITT profiles of both LFPs during charge and discharge. The black dotted lines represent the equilibrium voltage of LFP vs. Li/Li$^+$. Consistent with the GITT measurement above, lithium-excess LFP shows considerably lower polarization from the equilibrium potential for both charge and discharge regardless of the duration of the rest time. However, with increasing rest time, the voltage profiles of lithium-excess LFP start to show an overshooting in the charge or discharge. In addition, the overshooting profile becomes more pronounced with additional rest time, as clearly observed in the insets of Fig. 5(f) and (g). The origin of the overshoot in LFP has not yet been clearly revealed yet, but it is believed that it results from the resistance involved in spinodal decomposition or nucleation formation from the pristine and electrochemically activated particles.[7] During the relaxation step, both LFPs would either undergo spinodal decomposition or relax back to the original state by exchanging lithium among each other or with particles in the Li-poor phase.[7,71] Since it is reported that the overshoots appear just before the sequential particle-by-particle process occurs and the full relaxation of particles is the triggering condition of
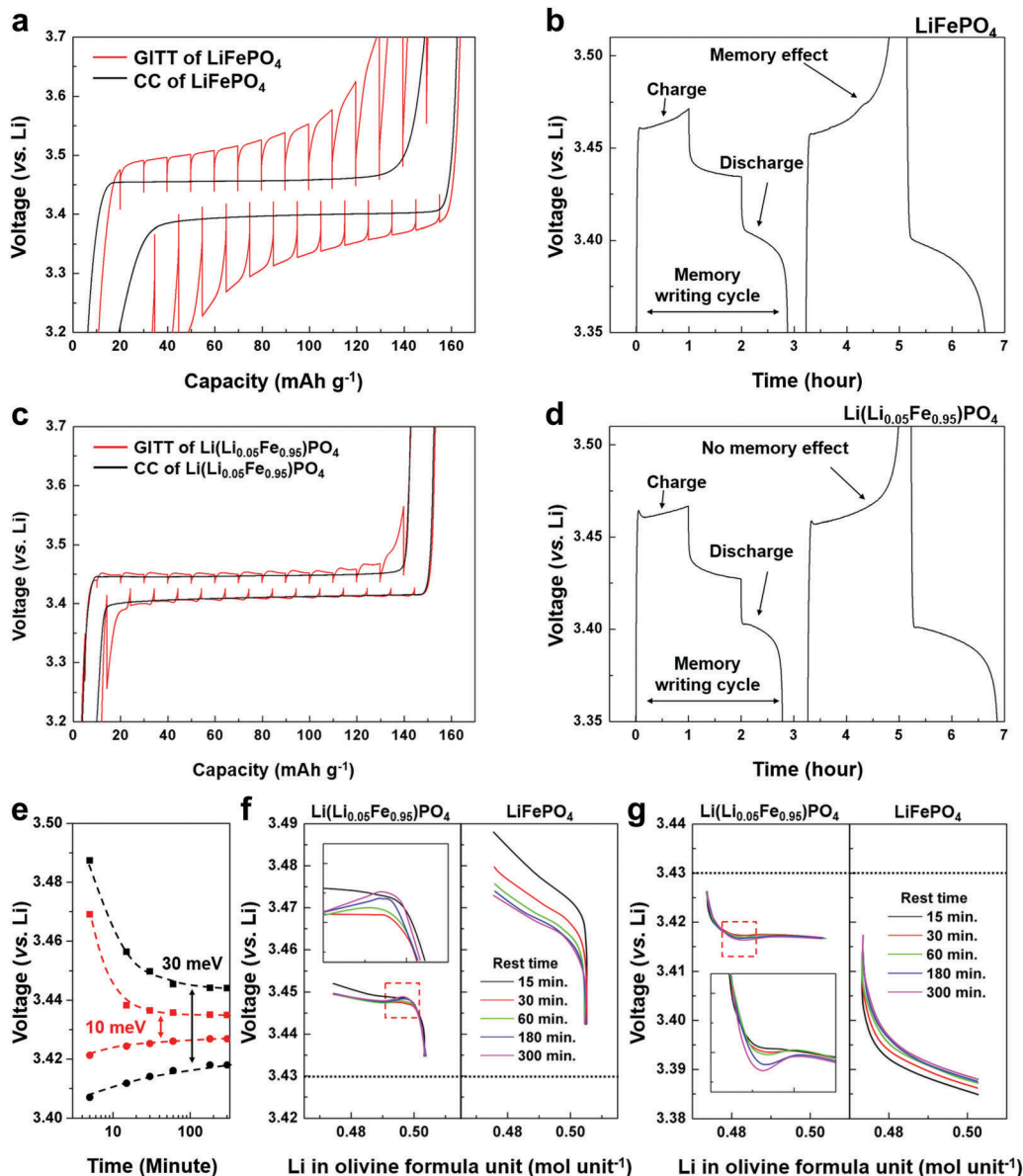
Fig. 5 Charge and discharge profile in CC (constant current) and GITT (galvanostatic intermittent titration technique) modes of (a) normal LFP and (c) lithium-excess LFP at a current rate of 10 mA g^{-1}. The rest time of GITT is about 20 minutes. (b and d) Show the memory effect test of both LFPs. Memory writing cycles (first cycle) are conducted to SOC 50% with one-hour rest time between charge and discharge. Memory releasing cycles (second cycle) are conducted within 2.5–4.5 V (vs. Li) with an 80 mA g^{-1} current rate. The memory effect is not observed in lithium-excess LFP. (e) OCV change of lithium-excess and normal LFPs as a function of rest time. (Black: normal LFP and red: lithium-excess LFP.) The lithium-excess LFP relaxed faster than normal LFP by reaching 10 mV charge and discharge OCV gaps. Partial GITT profile change depending on the rest times at each electrode during (f) charge and (g) discharge. Each inset figure exhibits the magnified profiles marked by red squares. The black dot line indicates the equilibrium potential of the LFP electrode vs. Li/Li$^+$.

the overshooting, the predominant overshooting is attributed to the faster relaxation kinetics of the lithium-excess LFPs. Nevertheless, the overshoot in lithium-excess LFP is relatively small. It is believed that the energy penalty that the particle needs to climb again would be less for lithium-excess LFP because of the reduced spinodal decomposition barrier, as indicated in Fig. 4(g), which would also reduce the overshooting during charge/discharge.

The results of the relaxation time vs. polarization experiments give us a hint as to why the memory effect is not observed in lithium-excess LFP. Sasaki et al. demonstrated that as the rest time

increases between the memory writing and memory releasing step, the memory effect is notably reduced because of sufficient time for homogenization of the lithium chemical potential among LFP particles.[7] This finding implies that how fast the electrode material relaxes to the stable state at zero current will sensitively affect the dominance of the memory effect. Accordingly, we designed an experiment on lithium-excess LFP to impose a shorter interval between the memory writing and releasing cycles. As we systematically decrease the interval from 10 min to 1 min in Fig. S26 (ESI†), the memory effect begins to appear. When the interval time

2912 | Energy Environ. Sci., 2016, 9, 2902–2915

This journal is © The Royal Society of Chemistry 2016

becomes less than 5 min, the signature of the voltage protrusion is observed even though the magnitude is significantly smaller than for normal LFP under the same conditions, indicating that the memory effect is a universal effect in olivine LFPs. However, because lithium-excess LFP allows much faster lithium kinetics, the homogenization of the lithium chemical potential among particles will also be significantly quicker after the memory writing step. Therefore, within the same interval, the homogenization would be far more efficient for lithium-excess LFP, and a detectable memory effect would not be observed.

Conclusions

In summary, we successfully synthesized a lithium-excess LFP, $Li(Li_{0.05}Fe_{0.95})PO_4$, using a solid-state method. The lithium-excess LFP exhibited unexpected physical and chemical properties that are remarkably distinguishable from those of normal LFP, which is primarily due to near-zero Fe_{Li} anti-site defects. The origin of the decreasing Fe_{Li} anti-site defect concentration is attributed to the destabilization of the Fe_{Li}-related defect formation in lithium-excess environments in the olivine framework. We demonstrated that the local lithium-excess configuration (i) provides additional lithium diffusion paths along the [101] directions, (ii) lowers the spinodal decomposition point and (iii) significantly weakens the memory effect. We believe that unlocking the restrictive lithium ion diffusion in the olivine electrode is expected to affect other intrinsic thermodynamic and kinetic properties of olivine LFPs, such as the phase boundary configuration, intermediate phase, and relaxation behavior, which requires further investigation. Notably, all of these physical changes in olivine cathodes originate from only a small change in Li/Fe compositions. Our results suggest that a simple lithium-excess concept in the electrode crystal not only enhances the power capability but also leads to unexpected properties for the pristine crystal and offers a novel interesting approach to tune solid-state ionic conductors.

Experimental

Materials and characterization

LFPs with various compositions were synthesized using Li_2CO_3 (Sigma Aldrich, 99.9%), $FeC_2O_4 \cdot H_2O$ (Sigma Aldrich, 99%), and $(NH_4)_2HPO_4$ (Aldrich, 98%). Each precursor was pulverized as fine as possible, separately using high-energy ball-milling in an Ar atmosphere to avoid oxidation. The fine precursors were mixed by wet ball milling using acetone for more than 24 hours. After drying the mixture, the powder was, again, pulverized as fine as possible using dry ball milling to obtain uniformity and calcinated at 350 °C with 5–6 °C min^{-1} heating rate for 10 hours. The calcinated powders were reground and pelletized under more than 300 bar. The final sintering process was conducted with a heating rate of 5–6 °C min^{-1} in an Ar atmosphere for 10 hours. High-resolution powder diffraction patterns were recorded using synchrotron X-ray radiation (the 8C2-HRPD beam-line at the Pohang Accelerator Laboratory, Korea). ND data

were collected using a high-resolution powder diffractometer (HRPD) at the HANARO facility of the Korea Atomic Energy Research Institute.

Calculation details

DFT calculations were performed using the Perdew Burke Ernzerhof (PBE) exchange–correlation parameterization with the spin-polarized generalized-gradient approximation (GGA). A plane-wave basis set and the projector-augmented wave (PAW) method as implemented in the Vienna *ab initio* simulation package (VASP) were used. We used a Hubbard U parameter of $U_{eff} = 4.3$ eV for Fe ions.[72–74] A kinetic energy cut-off of the plane-wave basis set was 500 eV and appropriate numbers of Monkhorst–Pack k-points were used. The calculation details are described in the ESI.†

Electrode preparation

Electrochemical cells were assembled in an Ar-filled glove box using a CR2032-type coin cell with Li metal as the counter electrode. A separator (GFF) and 1 M $LiPF_6$ in ethyl carbonate/dimethyl carbonate (Panax, EC/DMC, 1 : 1 v/v) as the electrolyte were used in cell fabrication. The electrodes' slurry was cast on Al foil using polyvinylidene fluoride (PVDF, as a binder, 10 wt%), super p (carbon, as a conductive agent, 20 wt%) and active materials (70 wt%) with a ~ 3.1 mg cm^{-2} active materials density.

Author contribution

K.-Y. Park and K. Kang designed the research and wrote the manuscript. K.-Y. Park designed and performed the experiments and analyzed the data. I. Park and G. Yoon conducted the DFT calculations and H. Kim, S. Lee and D. Ahn conducted structural analysis. Y. Cho, Y. Yun, J.-J. Kim, H. Kim, I. Hwang and Y. Kim contributed to electrochemical experiments and surface analysis. All authors discussed the experiments and contributed to writing the manuscript. K. K. guided all aspects of the work.

Acknowledgements

Notes and references

1 M. Armand and J. M. Tarascon, *Nature*, 2008, **451**, 652–657.
2 G. H. Vineyard and G. J. Dienes, *Phys. Rev.*, 1954, **93**, 265–268.
3 M. S. Islam, D. J. Driscoll, C. A. J. Fisher and P. R. Slater, *Chem. Mater.*, 2005, **17**, 5085–5092.
4 J. Wang, J. Yang, Y. Tang, J. Liu, Y. Zhang, G. Liang, M. Gauthier, Y.-c. Karen Chen-Wiegart, M. Norouzi Banis,

This journal is © The Royal Society of Chemistry 2016

Energy Environ. Sci., 2016, **9**, 2902–2915 | 2913

X. Li, R. Li, J. Wang, T. K. Sham and X. Sun, *Nat. Commun.*, 2014, **5**, 3415.

5 J. Chen and J. Graetz, *ACS Appl. Mater. Interfaces*, 2011, **3**, 1380–1384.

6 C. Delmas, J. P. Pérès, A. Rougier, A. Demourgues, F. Weill, A. Chadwick, M. Broussely, F. Perton, P. Biensan and P. Willmann, *J. Power Sources*, 1997, **68**, 120–125.

7 T. Sasaki, Y. Ukyo and P. Novák, *Nat. Mater.*, 2013, **12**, 569–575.

8 Y. Li, F. El Gabaly, T. R. Ferguson, R. B. Smith, N. C. Bartelt, J. D. Sugar, K. R. Fenton, D. A. Cogswell, A. L. D. Kilcoyne, T. Tyliszczak, M. Z. Bazant and W. C. Chueh, *Nat. Mater.*, 2014, **13**, 1149–1156.

9 P. Gibot, M. Casas-Cabanas, L. Laffont, S. Levasseur, P. Carlach, S. Hamelet, J.-M. Tarascon and C. Masquelier, *Nat. Mater.*, 2008, **7**, 741–747.

10 C. Delmas, M. Maccario, L. Croguennec, F. Le Cras and F. Weill, *Nat. Mater.*, 2008, **7**, 665–671.

11 P. Bai and M. Z. Bazant, *Nat. Commun.*, 2014, **5**, 3585.

12 C. Delacourt, P. Poizot, J.-M. Tarascon and C. Masquelier, *Nat. Mater.*, 2005, **4**, 254–260.

13 A. K. Padhi, K. S. Nanjundaswamy and J. B. Goodenough, *J. Electrochem. Soc.*, 1997, **144**, 1188–1194.

14 M. Nishijima, T. Ootani, Y. Kamimura, T. Sueki, S. Esaki, S. Murai, K. Fujita, K. Tanaka, K. Ohira, Y. Koyama and I. Tanaka, *Nat. Commun.*, 2014, **5**, 4553.

15 A. Yamada, S. C. Chung and K. Hinokuma, *J. Electrochem. Soc.*, 2001, **148**, A224–A229.

16 S.-i. Nishimura, G. Kobayashi, K. Ohoyama, R. Kanno, M. Yashima and A. Yamada, *Nat. Mater.*, 2008, **7**, 707–711.

17 R. Malik, D. Burch, M. Bazant and G. Ceder, *Nano Lett.*, 2010, **10**, 4123–4127.

18 C. Tealdi, C. Spreafico and P. Mustarelli, *J. Mater. Chem.*, 2012, **22**, 24870–24876.

19 S.-Y. Chung, S.-Y. Choi, T. Yamamoto and Y. Ikuhara, *Phys. Rev. Lett.*, 2008, **100**, 125502.

20 J. Chen, M. J. Vacchio, S. Wang, N. Chernova, P. Y. Zavalij and M. S. Whittingham, *Solid State Ionics*, 2008, **178**, 1676–1693.

21 S. Yang, P. Y. Zavalij and M. Stanley Whittingham, *Electrochem. Commun.*, 2001, **3**, 505–508.

22 J. Chen and M. S. Whittingham, *Electrochem. Commun.*, 2006, **8**, 855–858.

23 K.-Y. Park, I. Park, H. Kim, H.-d. Lim, J. Hong, J. Kim and K. Kang, *Chem. Mater.*, 2014, **26**, 5345–5351.

24 A. V. Radhamani, C. Karthik, R. Ubic, M. S. Ramachandra Rao and C. Sudakar, *Scr. Mater.*, 2013, **69**, 96–99.

25 S. Yuan and K. Dai, *Russ. J. Electrochem.*, 2014, **50**, 385–389.

26 K. Hoang and M. Johannes, *Chem. Mater.*, 2011, **23**, 3003–3013.

27 R. Amisse, S. Hamelet, D. Hanzel, M. Courty, R. Dominko and C. Masquelier, *J. Electrochem. Soc.*, 2013, **160**, A1446–A1450.

28 S. Hamelet, M. Casas-Cabanas, L. Dupont, C. Davoisne, J. M. Tarascon and C. Masquelier, *Chem. Mater.*, 2011, **23**, 32–38.

29 R. Amisse, M. T. Sougrati, L. Stievano, C. Davoisne, G. Dražič, B. Budič, R. Dominko and C. Masquelier, *Chem. Mater.*, 2015, **27**, 4261–4273.

30 S.-Y. Chung, S.-Y. Choi, T.-H. Kim and S. Lee, *ACS Nano*, 2015, **9**, 850–859.

31 M. E. Schuster, D. Teschner, J. Popovic, N. Ohmer, F. Girgsdies, J. Tornow, M. G. Willinger, D. Samuelis, M.-M. Titirici, J. Maier and R. Schlögl, *Chem. Mater.*, 2013, **26**, 1040–1047.

32 C. M. Julien, A. Mauger and K. Zaghib, *J. Mater. Chem.*, 2011, **21**, 9955–9968.

33 A. R. Armstrong, C. Lyness, P. M. Panchmatia, M. S. Islam and P. G. Bruce, *Nat. Mater.*, 2011, **10**, 223–229.

34 Z. Lu, D. D. MacNeil and J. R. Dahn, *Electrochem. Solid-State Lett.*, 2001, **4**, A191–A194.

35 N. Yabuuchi, K. Yoshii, S.-T. Myung, I. Nakai and S. Komaba, *J. Am. Chem. Soc.*, 2011, **133**, 4404–4419.

36 E. Salager, V. Sarou-Kanian, M. Sathiya, M. Tang, J.-B. Leriche, P. Melin, Z. Wang, H. Vezin, C. Bessada, M. Deschamps and J.-M. Tarascon, *Chem. Mater.*, 2014, **26**, 7009–7019.

37 M. Sathiya, K. Ramesha, G. Rousse, D. Foix, D. Gonbeau, A. S. Prakash, M. L. Doublet, K. Hemalatha and J. M. Tarascon, *Chem. Mater.*, 2013, **25**, 1121–1131.

38 J. Ma, Y.-N. Zhou, Y. Gao, X. Yu, Q. Kong, L. Gu, Z. Wang, X.-Q. Yang and L. Chen, *Chem. Mater.*, 2014, **26**, 3256–3262.

39 M. Sathiya, A. M. Abakumov, D. Foix, G. Rousse, K. Ramesha, M. Saubanère, M. L. Doublet, H. Vezin, C. P. Laisa, A. S. Prakash, D. Gonbeau, G. VanTendeloo and J. M. Tarascon, *Nat. Mater.*, 2015, **14**, 230–238.

40 M. Sathiya, G. Rousse, K. Ramesha, C. P. Laisa, H. Vezin, M. T. Sougrati, M. L. Doublet, D. Foix, D. Gonbeau, W. Walker, A. S. Prakash, M. Ben Hassine, L. Dupont and J. M. Tarascon, *Nat. Mater.*, 2013, **12**, 827–835.

41 J. Lee, A. Urban, X. Li, D. Su, G. Hautier and G. Ceder, *Science*, 2014, **343**, 519–522.

42 M.-S. Yoon, M. Islam, Y. Park, S. Hoon, J.-T. Son and S.-C. Ur, *Met. Mater. Int.*, 2014, **20**, 785–791.

43 W. Huang, Q. Cheng and X. Qin, *Russ. J. Electrochem.*, 2010, **46**, 359–362.

44 H. Kim, S. Lee, Y.-U. Park, H. Kim, J. Kim, S. Jeon and K. Kang, *Chem. Mater.*, 2011, **23**, 3930–3937.

45 G. X. Wang, S. Bewlay, S. A. Needham, H. K. Liu, R. S. Liu, V. A. Drozd, J.-F. Lee and J. M. Chen, *J. Electrochem. Soc.*, 2006, **153**, A25–A31.

46 M. Giorgetti, M. Berrettoni, S. Scaccia and S. Passerini, *Inorg. Chem.*, 2006, **45**, 2750–2757.

47 B. Kang and G. Ceder, *Nature*, 2009, **458**, 190–193.

48 K. Zaghib, J. Goodenough, A. Mauger and C. Julien, *J. Power Sources*, 2009, **194**, 1021–1023.

49 G. Ceder and B. Kang, *J. Power Sources*, 2009, **194**, 1024–1028.

50 J. Cabana, J. Shirakawa, G. Chen, T. J. Richardson and C. P. Grey, *Chem. Mater.*, 2010, **22**, 1249–1262.

51 M. C. Tucker, M. M. Doeff, T. J. Richardson, R. Fiñones, E. J. Cairns and J. A. Reimer, *J. Am. Chem. Soc.*, 2002, **124**, 3832–3833.

2914 | *Energy Environ. Sci.*, 2016, **9**, 2902–2915

This journal is © The Royal Society of Chemistry 2016

52 S. Upreti, N. A. Chernova, J. Xiao, J. K. Miller, O. V. Yakubovich, J. Cabana, C. P. Grey, V. L. Chevrier, G. Ceder, J. L. Musfeldt and M. S. Whittingham, *Chem. Mater.*, 2011, **24**, 166–173.

53 L. J. M. Davis, I. Heinmaa and G. R. Goward, *Chem. Mater.*, 2010, **22**, 769–775.

54 S. Hamelet, P. Gibot, M. Casas-Cabanas, D. Bonnin, C. P. Grey, J. Cabana, J.-B. Leriche, J. Rodriguez-Carvajal, M. Courty, S. Levasseur, P. Carlach, M. Van Thournout, J.-M. Tarascon and C. Masquelier, *J. Mater. Chem.*, 2009, **19**, 3979–3991.

55 F. Omenya, N. A. Chernova, S. Upreti, P. Y. Zavalij, K.-W. Nam, X.-Q. Yang and M. S. Whittingham, *Chem. Mater.*, 2011, **23**, 4733–4740.

56 A. R. Armstrong, M. Holzapfel, P. Novák, C. S. Johnson, S.-H. Kang, M. M. Thackeray and P. G. Bruce, *J. Am. Chem. Soc.*, 2006, **128**, 8694–8698.

57 D. Morgan, A. Van der Ven and G. Ceder, *Electrochem. Solid-State Lett.*, 2004, **7**, A30–A32.

58 K. Kang and G. Ceder, *Phys. Rev. B: Condens. Matter Mater. Phys.*, 2006, **74**, 094105.

59 A. Van der Ven and G. Ceder, *Electrochem. Solid-State Lett.*, 2000, **3**, 301–304.

60 G. K. P. Dathar, D. Sheppard, K. J. Stevenson and G. Henkelman, *Chem. Mater.*, 2011, **23**, 4032–4037.

61 R. Tripathi, G. R. Gardiner, M. S. Islam and L. F. Nazar, *Chem. Mater.*, 2011, **23**, 2278–2284.

62 K. Rissouli, K. Benkhouja, J. R. Ramos-Barrado and C. Julien, *J. Mater. Sci. Eng. B*, 2003, **98**, 185–189.

63 P. Bai, D. A. Cogswell and M. Z. Bazant, *Nano Lett.*, 2011, **11**, 4890–4896.

64 K.-Y. Park, J. Hong, J. Kim, Y.-U. Park, H. Kim, D.-H. Seo, S.-W. Kim, J.-W. Choi and K. Kang, *J. Electrochem. Soc.*, 2013, **160**, A444–A448.

65 D. Choi and P. N. Kumta, *J. Power Sources*, 2007, **163**, 1064–1069.

66 C. Zhu, Y. Yu, L. Gu, K. Weichert and J. Maier, *Angew. Chem., Int. Ed.*, 2011, **50**, 6278–6282.

67 S. W. Oh, S.-T. Myung, S.-M. Oh, K. H. Oh, K. Amine, B. Scrosati and Y.-K. Sun, *Adv. Mater.*, 2010, **22**, 4842–4845.

68 D. Lepage, C. Michot, G. Liang, M. Gauthier and S. B. Schougaard, *Angew. Chem., Int. Ed.*, 2011, **50**, 6884–6887.

69 B. Wang, W. Al Abdulla, D. Wang and X. S. Zhao, *Energy Environ. Sci.*, 2015, **8**, 869–875.

70 R. Malik, F. Zhou and G. Ceder, *Nat. Mater.*, 2011, **10**, 587–590.

71 W. Dreyer, J. Jamnik, C. Guhlke, R. Huth, J. Moskon and M. Gaberscek, *Nat. Mater.*, 2010, **9**, 448–453.

72 J. P. Perdew, K. Burke and M. Ernzerhof, *Phys. Rev. Lett.*, 1996, **77**, 3865–3868.

73 G. Kresse and J. Furthmüller, *Comput. Mater. Sci.*, 1996, **6**, 15–50.

74 V. I. Anisimov, J. Zaanen and O. K. Andersen, *Phys. Rev. B: Condens. Matter Mater. Phys.*, 1991, **44**, 943–954.